Projective Parallel Single-pixel Imaging to Overcome Global Illumination in 3D Structure Light Scanning

Yuxi Li[1][0000−0002−1922−5811], Huijie Zhao[2], Hongzhi Jiang[1], and Xudong Li[1]

[1] School of Instrumentation and Optoelectronic Engineering, Beihang University (BUAA), Beijing, China
uniluxli@qq.com, {jhz1862,xdli}@buaa.edu.cn
[2] Institute of Artificial Intelligence, Beihang University (BUAA), Beijing, China
hjzhao@buaa.edu.cn

Abstract. We consider robust and efficient 3D structure light scanning method in situations dominated by global illumination. One typical way of solving this problem is via the analysis of 4D light transport coefficients (LTCs), which contains complete information for a projector–camera pair, and is a 4D data set. However, the process of capturing LTCs generally takes long time. We present projective parallel single-pixel imaging (pPSI), wherein the 4D LTCs are reduced to multiple projection functions to facilitate a highly efficient data capture process. We introduce local maximum constraint, which provides necessary condition for the location of correspondence matching points when projection functions are captured. Local slice extension method is introduced to further accelerate the capture of projection functions. We study the influence of scan ratio in local slice extension method on the accuracy of the correspondence matching points, and conclude that partial scanning is enough for satisfactory results. Our discussions and experiments include three typical kinds of global illuminations: inter-reflections, subsurface scattering, and step edge fringe aliasing. The proposed method is validated in several challenging scenarios.

Keywords: Global illumination · 3D reconstruction · Single-pixel imaging

1 Introduction

A common assumption in structure light scanning (SLS) methods, such as fringe projection profilometry (FPP) [34][35][8] and grey coding [12], is that light ray only travels along a direct path when transmitting through a scene. Therefore, SLS methods are susceptible to systematic distortions and random errors when global illumination exists between projector pixels and a camera pixel [32][31][16][33][13]. Global illumination can occur when the investigated objects embody complicated surfaces and materials. For instance, inter-reflections, as shown in Fig. 1(a), dominate between highly glossy reflective surfaces. In these surfaces, the light beams received by camera pixels contain not only directly reflected light, but also inter-reflected light between surfaces. Subsurface scattering effects, as shown in Fig.1(b), arise at translucent surfaces when light penetrates the surface and exits at different positions around the incident point. Fringe aliasing occurs at positions with discontinued structures, such as step edge, wherein a camera pixel can simultaneously observe the foreground and background when the edge slice exactly passes through the pixel, as shown in Fig. 1(c). Analyzing and decomposing the influences caused by global illuminations through modern cameras is a challenging and open problem [22].

Light transport equation describes the complex transport behavior between projector pixels and camera pixels. The path between the projector and camera pixels can be determined by capturing and analyzing light transport coefficients (LTCs) [13], which denote the light radiance between every possible projector and camera positions combinations; this process enables correspondence matching because the direct path can be identified. However, LTCs are a 4D dataset, which parameterizes light rays in terms of a 2D camera and 2D projector coordinates. Thus, LTCs involve huge data volume, and capturing them takes long time. LTCs can be visualized by a 2D image with projector resolutions, given a camera pixel. We refer to the 2D image with projector resolutions as pixel transport image.

As a step toward a robust and efficient analysis of light transport behavior, we develop projective parallel single-pixel imaging (pPSI) to separate the influences of lights caused by global illumination in 3D scanning. Provided that only the correspondence point is the ultimate goal in 3D reconstruction, LTCs contains over-complete information because only the direct correspondence point is extracted and stored. In the present paper, we show that the correspondence matching position can be obtained when the projection function(s) of the pixel transport image is captured, through the local maximum constraint.

1.1 Contributions

We introduce pPSI, which is a robust, efficient and comprehensive method of 3D reconstruction in the presence of global illumination. Rather than capturing complete 4D LTCs, pPSI captures multiple projection functions, thereby enabling highly efficient data capture procedure. The local maximum constraint is proven, which states that the correspondence matched point (direct illumination point) on the pixel transport image is retained as the local maximum on the projection function(s). We introduce oblique sinusoidal pattern illumination mode to capture projection functions, and correspondence point can be calculated by intersecting the lines that satisfy the local maximum constraint. Local slice extension method, which involves a "coarse to fine" localization procedure, is introduced for highly efficient projective function capture. Experimental results show that partial frequency scanning can obtain satisfactory results, which enables 3D reconstruction under global illumination with a few hunderds patterns. Three kinds of global illuminations are discussed, namely inter-reflections, subsurface scattering and step edge fringe aliasing (Fig. 1). For step edge fringe aliasing, the upper edge illumination is referred to as direct illumination, and the lower edge illumination as global illumination.

The present paper offers the following contributions.

1. We develop pPSI, which is a robust, efficient and comprehensive model for analyzing and solving global illumination effects. Local slice extension method is introduced for highly efficient capture of projection functions.

2. The relationship between projection functions and LTCs is demonstrated theoretically, and the oblique sinusoidal pattern illumination mode is proposed.

3. The local maximum constraint is introduced for candidate calculation, and the fundamental principle is proven both theoretically and experimentally.

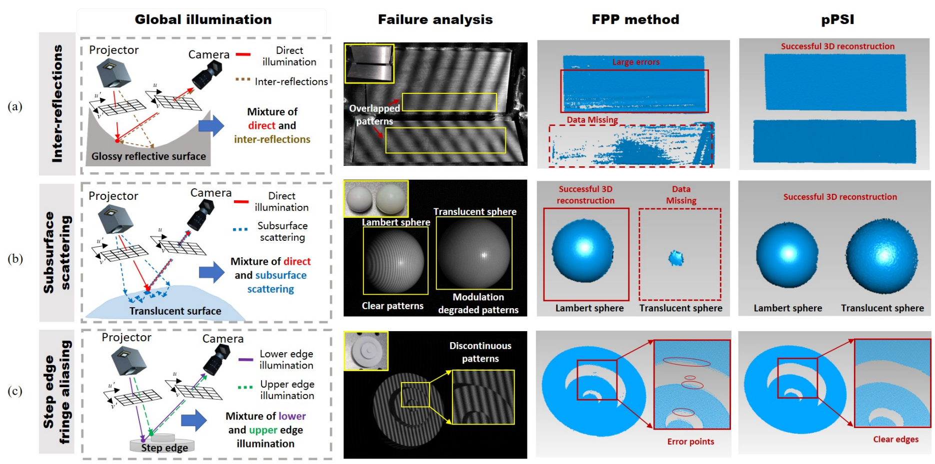

Fig. 1. Global illumination problems discussed in this study. Typical global illumination effects include (a) inter-reflections, (b) subsurface scattering, and (c) step edge fringe aliasing. Inter-reflections incurs overlapped pattern. Subsurface scattering degrades the modulation of the patterns, and step edges cause discontinuous patterns. Global illumination effects cause failure in traditional SLS methods, such as FPP. However, our method (pPSI) can solve these problems both robustly and efficiently.

2 Related Work

2.1 3D Reconstruction under Global Illumination

Several methods are developed to solve 3D reconstruction under global illuminations; these methods include high-frequency projection methods [21][2][10][9], regional projection methods [11][17][29][30], and polarization projection methods [1][4]. However, these methods are based on specific assumptions that may not be satisfied in real applications. For example, high frequency projection methods such as modulated phase-shifting [2] and mircro-phase shifting [10] are mainly to suppress lower frequency inter-reflections. These methods used high frequency patterns and are based on an assumption: only low frequency global illumination exist, which fails in practical situations. O'Tool et al. [22] introduced structured light transport (SLT) method for 3D reconstruction under global illumination. However, non-epipolar assumption was made in SLT, which assumes that epipolar indirect illumination is not strong. In many real world applications, this assumption can be broken when epipolar plane reflection is strong. On the contrary, pPSI makes no explicit assumption and handles inter-reflections (espically specular inter-reflections) and strong subsurface scattering simultaneously.

Recently, several 3D reconstruction methods that assume no explicit assumption to overcome global illumination are introduced. Park et al. [24] proposed multipeak range imaging. However, this method requires long capture time, since each projector stripe line has to be illuminated in turn. In pPSI, each camera pixel is treated as an independent unit, and reconstructs a 1D projection function. Each measured pixel value has whole information of projection function. Thus, the excellent compressive properity of Fourier single-pixel imaging can be explored, and the projection number can be reduced largely. Recently, Diezu et al. [6] proposed a method called frequency shift triangulation. However, this method requires a calibration process to determine the minimal phase step of the measurement system, and uses a dynamic programming method to eliminate erroneous data for successful 3D reconstruction. Zhang et al. [32] introduced a general mathematical model to solve 3D reconstruction under global illumination. Later, Zhang et al. [31] introduced a sparse multi-path correction method. However, this method requires an iterative optimization process, which can prolong the calculation time and is not suitable for parallel computing. On the contrary, pPSI requires no additional calibration stage, and the reconstruction algorithm requires no iterative process, which is suitable for parallel computing.

2.2 Light Transport Coefficients Capture

Light transport is important for computer vision and graphics. Debevec et al. [5] introduced the capture of a simplified 4D light transport function by a light stage. Masselus et al. [20] proposed the use of a projector–camera system to capture a 6D slice of the full light transport function. These early methods directly capture LTCs, which results in a relatively low capture speed.

Adaptive methods, such as dual photography [26] and symmetric photography[7], and compressive imaging methods [27][25][3] are introduced for highly efficient light transport capture. However, these methods either require a complex illumination mode or a complex reconstruction algorithm. Primal–dual coding [23] and SLT [22] are developed, wherein both the illumination and camera pixels are controlled simultaneously to manipulate different components in the light transport between the projector and the camera. However, this method requires special optical design and hardware.

A single-pixel imaging method is developed for LTCs capture[16][15]. Jiang et al. [13] introduced parallel single-pixel imaging (PSI) for efficient LTCs capture using the local region extension (LRE) method. A compressive PSI [19]is also introduced for highly efficient LTCs capture. PSI is extended to paraxial systems [28], and for separating higher order inter-reflections [14]. This work is an extension to the work by Jiang et al. [13].

In the present paper, we aim to achieve robust and efficient correspondence matching under strong global illumination for 3D scanning. The most outstanding feature of pPSI is that pPSI provides good balance between robustness and efficiency in 3D reconstruction under global illumination. The robustnesss means that pPSI makes no explicit assumption and handles inter-reflections (specular) and strong subsurface scattering simultaneously. The efficiency means that pPSI captures projection functions rather than LTCs. This makes pPSI more efficient than the methods that capture LTCs to solve 3D reconstruction under global illumination. In the present paper, we take advantage of the excellent compressive property of Fourier spectrum, and achieve 3D reconstruction with a few hundreds patterns (336 pattterns).

3 Background

PSI captures LTCs $h(u', v'; u, v)$, which are a 4D dataset, between projector pixel (u', v') and camera pixel (u, v). LTCs describe the image forming process, which is expressed as

$$I(u, v) = O(u, v) + \sum_{v'=0}^{N-1} \sum_{u'=0}^{M-1} h(u', v'; u, v) P(u', v'), \tag{1}$$

where $I(u, v)$ is the radiance captured by camera pixel (u, v), $O(u, v)$ is the environment illumination, $P(u', v')$ is the illuminated radiance of projector pixel (u', v'). M and N are the horizontal and vertical resolution of the projector, respectively.

Jiang et al. [13] introduced the LRE method to accelerate the capture efficiency of PSI; this method assumes that the visible region of each pixel is confined in a local region; they proved the perfect reconstruction property of LRE. Reference [13] provides detailed information on PSI. In the present paper, we refer to the visible region as reception field.

4 Projective Parallel Single-pixel Imaging for Efficient Separation of Direct and Global Illumination

4.1 Local Maximum Constraint Proposition

This section provides the basics for obtaining direct illumination point (correspondence matched point) via projection functions. PSI requires complete LTCs capture. However, in the case of 3D reconstruction, LTCs contain over-complete information because only the direct correspondence point is extracted and stored. The key observation underlying pPSI is that the direct illumination point can be recovered if the 1D projection function(s) of the pixel transport image is captured [Fig. 2(a)]

$$\begin{aligned} f_\theta^{Radon}(\rho; u, v) &= \Re_\theta[h(u', v'; u, v)] \\ &= \sum_{v'=0}^{N-1} \sum_{u'=0}^{M-1} \cdot h(u', v'; u, v) \cdot \delta(\rho - u' \cos\theta - v' \sin\theta), \end{aligned} \tag{2}$$

where $\Re_\theta[h(u', v'; u, v)]$ is the discrete Radon transform of LTCs along direction θ, which is the angle between the integral direction of the projection function and horizontal axis, ρ is the coordinate of the projection function, $\delta(\bullet)$is the Dirac delt function. When each camera pixel is considered, $f_\theta(\rho; u, v)$ forms a 3D data cube.

We provide some definitions that are useful in following description. Angle θ defines the direction line to which the pixel transport image is projected. The direction line is obtained through counter-clockwise rotation of the horizontal axis by θ, as shown in Fig. 2(a). Given a direction line and a point (u', v'), projection line is defined as the line passing through point (u', v') and vertical to the direction line. Thus, the projection position of (u', v') to the direction line is the intersection of the projection line and the direction line, as shown in Fig. 2(a).

The fundamental principle for recovering direct illumination points given the projection functions is the local maximum constraint proposition, which provides constraint for the location of the correspondence matched point (direct illumination point) in the pixel transport image [Fig. 2(b)].

Theorem 1. *Local Maximum Constraint Proposition. The direct illumination point on the pixel transport image is a local maximum point on the projection functions, if the corresponding projection line does not pass through any speckles caused by global illumination.*

Proof of Local Maximum Constraint Proposition can be found in supplementary material. □

Local maximum constraint proposition provides a necessary condition for the location of correspondence matched points. Figs. 2 (a) and (b) provide an intuitive explanation of local maximum constraint proposition. Suppose multiple projection functions $f_\theta(\rho; u, v)$ with D directions are obtained, with the direction angle of d-th projection at θ_d. The d-th projection function has a total of T_d local maximums. The j-th local maximum of the d-th projection function is denoted as ρ_d^j. A grayscale centroid subpixel matching processing is introduced in [16] and [15], which should be applied to obtain ρ_d^j. The candidate correspondence matched points are calculated by solving the following linear equations

$$\begin{pmatrix} \cos\theta_1 & \sin\theta_1 & -\rho_1^m \\ \cos\theta_2 & \sin\theta_2 & -\rho_2^n \\ & \vdots & \\ \cos\theta_D & \sin\theta_D & -\rho_D^p \end{pmatrix} \begin{pmatrix} u' \\ v' \\ 1 \end{pmatrix} = \begin{pmatrix} 0 \\ 0 \\ \vdots \\ 0 \end{pmatrix}, \tag{3}$$

where m, n, p are integers, and take any combination that satisfy $m \in [0, T_1)$, $n \in [0, T_2)$, and $p \in [0, T_D)$. Each possible combination of local maximum in every projection line is formed and intersected according to Eq. (3), which can be solved by singular value decomposition (SVD). Not intersected combinations are eliminated by check of the rank. The ultimate correspondence matched points are then determined by the epipolar constraint between the projector and camera, as conducted in [13]-[16][19][28][33].

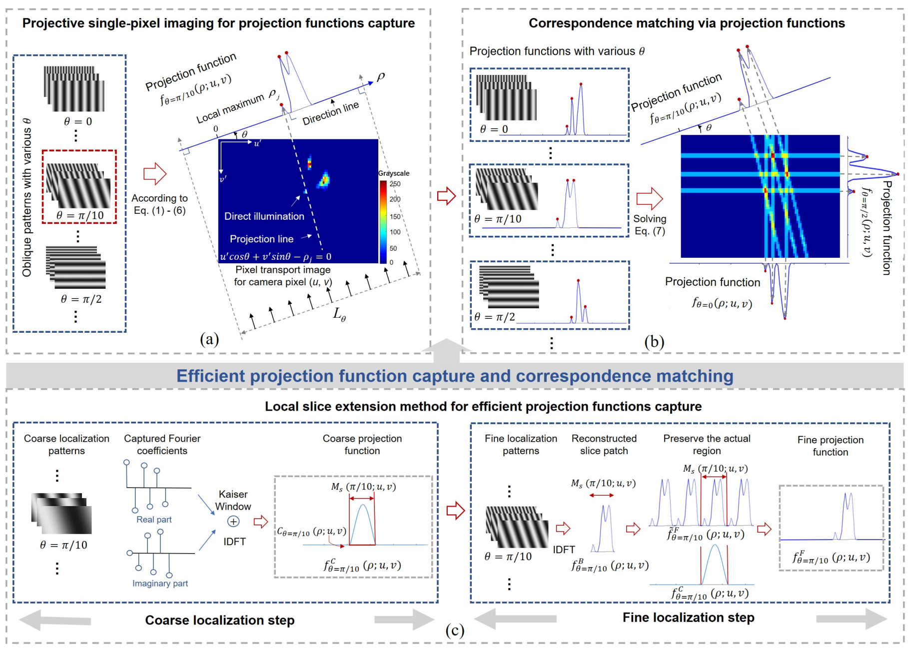

Fig. 2. Fundamental principles of pPSI. (a) Projective single-pixel imaging for projection functions capture. The illumination of oblique patterns is equivalent to the application of Radon transform to pixel transport image. The correspondence matching points of pixel transport image are retained in the projection functions (red spots). (b) Correspondence matching via projection functions. The red spots are local maximum. (c) Local slice extension method for efficient projection functions capture.

4.2 Projective Single-pixel Imaging for Projection Functions Capture

In this section, we show that illuminating oblique sinusoidal patterns is equivalent to applying Radon transform to the pixel transport image. Fig.2 (a) provides the basic idea.

If the oblique S-step ($S \geq 3$) sinusoidal patterns with following form are illuminated

$$P_i(u', v'; k, \theta) = a + b \cdot \cos[\frac{2\pi k}{L_\theta}(u' \cos\theta + v' \sin\theta) + \frac{2\pi i}{S}], \tag{4}$$

where i denotes the phase step, and take values of i=$0, 1, \ldots S-1$. a and b are the average and contrast of the patterns. k is the discrete frequency samples, and take values of k=$0, 1 \ldots K$, and $K \leq L_\theta$. L_θ is the equivalent projector resolution in the projector range for the directional projection function with an angle of θ [Fig. 2(a)], which can be calculated as

$$L_\theta = \begin{cases} \lceil M \cdot \cos\theta + N \cdot \sin\theta \rceil & 0 \leq \theta \leq \pi/2 \\ \lceil -M \cdot \cos\theta + N \cdot \sin\theta \rceil & \pi/2 < \ \theta < \pi \end{cases} \tag{5}$$

where $\lceil \centerdot \rceil$ is the ceiling function.

According to Eq. (1), the captured intensity for camera pixel (u, v) can be calculated as

$$\begin{aligned} I_i(u, v; k, \theta) = O(u, v) &+ \sum_{v'=0}^{N-1} \sum_{u'=0}^{M-1} a \cdot h(u', v'; u, v) \\ &+ \sum_{v'=0}^{N-1} \sum_{u'=0}^{M-1} b \cdot h(u', v'; u, v) \cdot \cos[\frac{2\pi k}{L_\theta}(u' \cos\theta + v' \sin\theta) + \frac{2\pi i}{S}]. \end{aligned} \tag{6}$$

Supposed that all of phase step i is captured, given a frequency sample k and an direction θ, we can obtain the following quantity

$$\begin{aligned} F_\theta(k; u, v) &= \sum_{i=0}^{S-1} I_i(u, v; k, \theta) \cos(2\pi i/S\ ) + j \sum_{i=0}^{S-1} I_i(u, v; k, \theta) \sin(2\pi i/S\ ) \\ &= \frac{S}{2} \cdot \sum_{v'=0}^{N-1} \sum_{u'=0}^{M-1} b \cdot h(u', v'; u, v) \cdot \exp[-\frac{2\pi k}{L_\theta}(u' \cos\theta + v' \sin\theta)]. \end{aligned} \tag{7}$$

Eq. (7) holds because the Lagrange's trigonometric identities. The product-to-sum formulas of trigonometric identities and the Euler's formula can then be applied.

When patterns with k=$0, 1 \ldots L_\theta - 1$ are illuminated, and $F_\theta(k; u, v)$ are calculated as Eq. (7), then, by taking IDFT to $F_\theta(k; u, v)$, the projection function $f_\theta(\rho; u, v)$, shown in Fig. 2, is obtained as

$$\begin{aligned} f_\theta(\rho; u, v) &= IDFT\{\frac{Sb}{2} \cdot \sum_{v'=0}^{N-1} \sum_{u'=0}^{M-1} \cdot h(u', v'; u, v) \cdot \exp[-\frac{2\pi k}{L_\theta}(u' \cos\theta + v' \sin\theta)]\} \\ &= \frac{Sb}{2} \cdot \sum_{r=-\infty}^{+\infty} \sum_{v'=0}^{N-1} \sum_{u'=0}^{M-1} \cdot h(u', v'; u, v) \cdot \delta(\rho - u' \cos\theta - v' \sin\theta - rL_\theta) \\ &= \frac{Sb}{2} \cdot \Re_\theta[h(u', v'; u, v)], \end{aligned} \tag{8}$$

where r are integers. Although $f_\theta(\rho;u,v)$ contains an infinite sum term, the pixel transport image has nonzero values only in one continuous region with length of L_θ. Thus, Eq. (8) is precisely applying discrete Radon transform to the pixel transport image along direction θ, with a scale factor. In the present paper, we use three-step sinusoidal oblique patterns for projection functions capture.

4.3 Local Slice Extension Method for Efficient Projection Functions Capture

Local slice extension method, which is implemented by a "coarse to fine" localization procedure, is introduced for highly efficient projection functions capture [Fig. 2(c)]. The fundamental basis of local slice extension method can be proven by reducing the LRE reconstruction theorem [13] to 1D case. Compared with the LRE method, local slice extension method captures projection functions with different orientations. Thus, in local slice extension method, concepts equivalent to the size and location of the reception field in LRE method are the size and location of the reception field projected along projection direction with θ. We refer to them as the size and location of θ projected reception field [Fig. 2(c)]. For implementation, focus should be on this section. Fig. 2(c) illustrates local slice extension method.

Coarse localization step This step has a two-fold goal, namely, detecting and obtaining the coarse location and size of the projected reception field. Oblique patterns with the form of Eq. (4) are projected. The obtained intensities are arranged as Eq. (7), and 1D IDFT is applied to the resulting quantities. A Kaiser window [18], wherein the shape parameter β is set as 5, is applied on the sampled low frequency samples to eliminate ringing effect. Coarse projection functions $f_\theta^C(\rho;u,v)$ can then be obtained. The coarse location of the projected reception field $C_\theta(\rho;u,v)$can be determined, which is a mask that has a value of one when the reconstructed coarse projection functions are greater than the noise threshold, and zero otherwise. The size of the projected reception field $M_s(\theta;u,v)$ is determined between the length in the first position greater than the noise threshold and the last position greater than the noise threshold. The number of frequencies for coarse localization is set as 10 in the present paper. Refer to supplementary material for a theoretical analysis of the relationship between localization accuracy and frequency number in the coarse localization step, and how the number of frequencies for coarse localization is chosen.

Fine localization step The fine projection patterns are in fact the 1D case of the periodic extension patterns introduced in reference [13]. Refer to supplementary material for detailed information on theoretical aspect of local slice extension method. Fine localization step contains three sub-steps.

First, the fine location patterns with the following form are projected

$$\tilde{P}_i(u',v';k,\theta) = a + b\cdot\cos[\frac{2\pi k_\theta}{M_\theta}(u'\cos\theta + v'\sin\theta) + \frac{2\pi i}{S}], \tag{9}$$

where θ is the angle between the integral direction of the projection function and horizontal axis. i denotes the phase step, and take values of i=0, 1, . . . $S - 1$. a and b are the average and contrast of the patterns. k is the discrete frequency samples, and takes the value of k_θ=0, 1 . . . $M_\theta - 1$. M_θ is the size of the maximum of θ projected reception field for each camera pixel, and is defined by

$$M_\theta = \max_{(u,v)} [M_s(\theta; u, v)]. \tag{10}$$

Due to the excellent compressive property of Fourier spectrum, partial frequencies can be used to obtain a satisfactory result. We tested the subpixel matched error with respect to different ratio of sampled frequencies, and chose a scan ratio of 25% in the present paper. This means that only the first 25 % frequencies are required to be captured. The unscanned frequencies are filled with zeros. Refer to supplementary material for detailed information.

Second, the captured intensities when each pattern is projected are arranged as Eq. (7), and 1D IDFT is applied to reconstruct slice patch $f_\theta^B(\rho; u, v)$. This reconstructed slice patch is then extended periodically for the projection functions with resolution of L_θ, and can be expressed by

$$\tilde{f}_\theta^F(\rho; u, v) = \sum_{r=0}^{\left\lceil \frac{L_\theta}{M\theta} \right\rceil} f_\theta^B(\rho - rM_\theta; u, v), \tag{11}$$

where r is integer, and ρ=0, 1 . . . $L_\theta - 1$.

Finally, the fine projection functions are reconstructed by preserving the nonzero region of $C_\theta(\rho; u, v)$ obtained from coarse localization step, as expressed by

$$f_\theta^r(\rho; u, v) = \tilde{f}_\theta^F(\rho; u, v) \centerdot C_\theta(\rho; u, v), \tag{12}$$

where $\centerdot$ denote the element-wise product.

Compared with PSI, the capture complexity of pPSI is reduced from O($M_s{}^2$) to O(M_s), where M_s is the size of the reception field.

5 Experiments and Evaluations

The experimental setup consisted of a camera and a projector (Fig. 1). The resolutions of the camera and projector are 1600×1200 and 1920×1080, respectively. The frame rate of the projector is synchronized with the frame rate of the camera. The capture rate of the system was 165 frames per second (fps). Several challenging scenarios were validated by pPSI. Refer to supplementary material for comparision of pPSI with micro-phase shifting.

5.1 Compound Scene

A compound scene, which contains a triangular groove and a candle, is used to compare pPSI and PSI. The image of the investigated scene is shown in Fig.

3(a). Oblique patterns with four orientations of θ=0°, 45°, 90°, 135°are projected. The length of the reception field for each direction was 150 according to the coarse localization step, which results in a total number of 336 patterns by pPSI. The steps for choosing the number of slices and the calculation of pattern number required by pPSI are provided in the supplementary material. Total acquisition time was 2 seconds. The reconstructed 3D shape is shown in Fig. 3(b). The number of patterns required by PSI is 51,000. Total acquisition time is about 5 minutes. Thus, pPSI provids about 150-fold improvement in the present experiment. The error map between pPSI and PSI is shown in Fig. 3(c). The root-mean-square (RMS) error is 0.023 (mm). This experiment illustrates that pPSI is both efficient and robust for 3D reconstruction in situations dominated by global illumination.

The LTCs for three typical points are shown in Figs. 3(e), (g) and (i). The coordinate of each correspondence point is also shown. We provided the coordinate of each correspondence point calculated by pPSI in Figs. 3 (d), (f) and (h). These correspondence points are calculated as intersection points of the projection lines, as shown in Figs. 3 (d), (f) and (h). The differences of these correspondence point calculated by pPSI and PSI are also shown.

5.2 Inter-reflections

In this subsection, pPSI is tested in situations dominated by inter-reflections. In the first scene, a gypsum bear was placed near a mirror [Fig. 4(a)]. High-frequency inter-reflections result in overlapped patterns, which is challenging for FPP. In the second scene [Fig. 4(b)], two metal blades were measured. The specular reflection also incurs overlapped patterns, which results in large data missing areas.

Oblique patterns with four orientations of θ=0°, 45°, 90°, 135°are projected for these two scenes. The length of the reception field for each direction was 150 according to the coarse localization step, which results in a total number of 336 patterns by pPSI. Total acquisition time was 2 seconds. Compared to PSI, pPSI achieved about 150-fold improvement in terms of acquisition time.

The accuracy of pPSI in situations dominated by inter-reflections is analyzed by a V-Groove that contains two metal gauge blocks [Fig. 5(a)]. A plane was fitted for the upper and lower plane separately. The RMS error between the fitted planes and data points of the upper plane and lower plane was 0.021 (mm) and 0.015 (mm), respectively.

5.3 Subsurface Scattering

In this subsection, pPSI is tested in situations dominated by subsurface scattering. In the first scene, a jade horse was investigated [Fig. 4(c)]. Strong subsurface scattering results in degraded patterns, which is challenging for FPP. In the second scene, a white onion and a pear was investigated. FPP method still failed to reconstruct satisfactory 3D shape. pPSI and PSI are able to reconstruct high quality 3D shapes for these two challenging scenes.

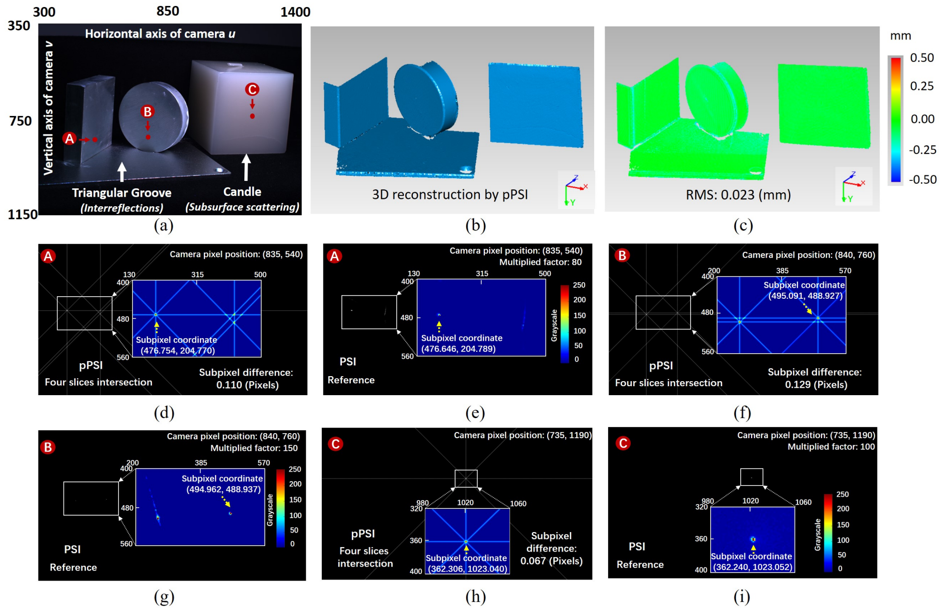

Fig. 3. Comparison between pPSI and PSI using the compound scene. (a) The compound scene contains inter-reflections and subsurface scattering. The camera coordinates are depicted. The positions of three points, namely points A, B, and C, are indicated by red circles. The intersection positions by pPSI and LTCs by PSI of these three points are shown in (d) – (i). (b) 3D shape reconstructed by pPSI. (c) Error map of the point cloud data between pPSI and PSI. RMS error was 0.023 mm. (d), (f) and (h) are the intersection points calculated by pPSI. The camera positions are indicated on the upper right corner. On the upper left corner of each of these subfigures, a circle with a letter inside indicates the point that corresponds to the subfigure. (e), (g) and (i) are the light transport coefficients and the subpixel matched positions calculated by PSI. The difference of the subpixel matched positions between pPSI and PSI are shown in (d), (f) and (h).

The measurement parameters are the same to that in Section 5.2. The number of projected patterns is 336. The difference between pPSI and PSI is negligible, but pPSI achieved about 150-fold improvement in terms of acquisition time.

The accuracy of pPSI in situations dominated by subsurface scattering is analyzed by a polyamide sphere with diameter of 25.449 (mm) [Fig. 5(b)]. A sphere was fitted by the reconstructd points. The RMS error between the fitted sphere and the reconstructed data points was 0.031 (mm), and the diameter of the fitted sphere was 25.432 (mm). Thus, the absolut reconstruction error of pPSI was 0.017mm, and the uncertainty of the measurement was 0.031mm.

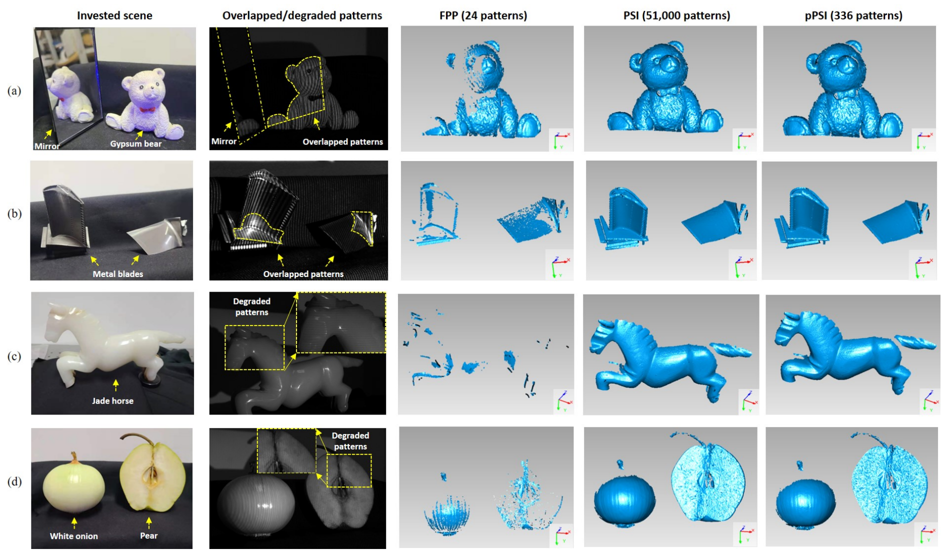

Fig. 4. Comparison of 3D shape reconstruction results among FPP, PSI and pPSI. The overlapped/degraded patterns are shown. (a) Gypsum bear. A mirror was placed near the bear such that high frequency strong inter-reflections dominate. (b) Metal blades. (c) Jade horse. (d) White onion and pear.

5.4 Step Edges

Fringe aliasing that occurs at step edges causes the missing data at step edges. We used three standard metal cylinder objects with diameters of 6.000 (mm), 7.000 (mm) and 8.000 (mm), as shown in Fig. 6(a), to test accuracy at step edges. The accuracy of the reconstructed diameter reflects the effect of the method used because the data points reconstructed by FPP tend to disappear near the step edges. The reconstructed results by FPP and pPSI are shown in Figs. 6(b)-(d). The black regions are the results reconstructed by FPP. The blue rings correspond to the area reconstructed by pPSI that were missed by FPP due to fringe aliasing at step edges. pPSI obtains more accurate results than FPP. The experimental data are summarized in Table 1.

6 Conclusion

In the present paper, pPSI is introduced for efficient and robust correspondence matching in instances dominated by global illumination. The relationship between LTCs and projection functions is demonstrated theoretically. The oblique sinusoidal pattern illumination mode is proposed. The local maximum constraint is introduced to identify the candidate correspondence points by intersecting the region that satisfies the local maximum constraint. Local slice extension method is introduced to further accelerate capture efficiency. Several challenging scenes

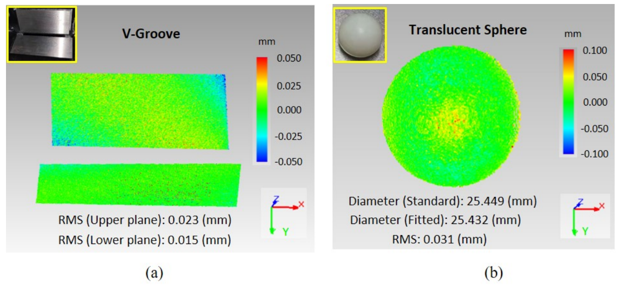

Fig. 5. Accuracy analysis of pPSI. (a) Accuracy analysis using V-Groove when interreflections are present. (b) Accuracy analysis using translucent sphere when subsurface scattering is present.

Table 1. Accuracy analysis data on metal cylinders

Diameter (mm)	FPP method		pPSI method	
	Measured Diameter (mm)	Absolute Error (mm)	Measured Diameter (mm)	Absolute Error (mm)
6.000	5.827	0.173	5.941	0.059
7.000	6.853	0.147	6.942	0.058
8.000	7.860	0.140	7.941	0.059

are measured and compared, which validates that pPSI achieves efficient and robust 3D shape measurement in the presence of global illumination.

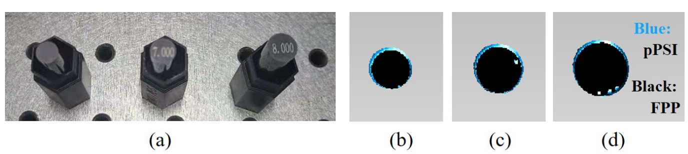

Fig. 6. Accuracy analysis by standard objects (step edges). (a) Cylinder standards. (b-d) The 3D data of the end surface. The pPSI results and FPP results are shown together. Black points correspond to FPP results, while blue points are pPSI results.

References

1. Chen, T., Lensch, H.P., Fuchs, C., Seidel, H.P.: Polarization and phase-shifting for 3d scanning of translucent objects. In: 2007 IEEE conference on computer vision and pattern recognition. pp. 1–8. IEEE (2007)
2. Chen, T., Seidel, H.P., Lensch, H.P.: Modulated phase-shifting for 3d scanning. In: 2008 IEEE Conference on Computer Vision and Pattern Recognition. pp. 1–8. IEEE (2008)
3. Chiba, N., Hashimoto, K.: 3d measurement by estimating homogeneous light transport (hlt) matrix. In: 2017 IEEE International Conference on Mechatronics and Automation (ICMA). pp. 1763–1768. IEEE (2017)
4. Clark, J., Trucco, E., Wolff, L.B.: Using light polarization in laser scanning. Image and Vision Computing **15**(2), 107–117 (1997)
5. Debevec, P., Hawkins, T., Tchou, C., Duiker, H.P., Sarokin, W., Sagar, M.: Acquiring the reflectance field of a human face. In: Proceedings of the 27th annual conference on Computer graphics and interactive techniques. pp. 145–156 (2000)
6. Dizeu, F.B.D., Boisvert, J., Drouin, M.A., Godin, G., Rivard, M., Lamouche, G.: Frequency shift triangulation: a robust fringe projection technique for 3d shape acquisition in the presence of strong interreflections. In: 2019 International Conference on 3D Vision (3DV). pp. 194–203. IEEE (2019)
7. Garg, G., Talvala, E.V., Levoy, M., Lensch, H.P.: Symmetric photography: Exploiting data-sparseness in reflectance fields. In: Rendering Techniques. pp. 251–262 (2006)
8. Gorthi, S.S., Rastogi, P.: Fringe projection techniques: whither we are? Optics and lasers in engineering **48**(ARTICLE), 133–140 (2010)
9. Gu, J., Kobayashi, T., Gupta, M., Nayar, S.K.: Multiplexed illumination for scene recovery in the presence of global illumination. In: International Conference on Computer Vision (2011)
10. Gupta, M., Nayar, S.K.: Micro phase shifting. In: 2012 IEEE Conference on Computer Vision and Pattern Recognition. pp. 813–820. IEEE (2012)
11. Hu, Q., Harding, K.G., Du, X., Hamilton, D.: Shiny parts measurement using color separation. Proceedings of SPIE - The International Society for Optical Engineering **6000**, 125–132 (2005)
12. Inokuchi, S.: Range imaging system for 3-d object recognition. ICPR, 1984 pp. 806–808 (1984)
13. Jiang, H., Li, Y., Zhao, H., Li, X., Xu, Y.: Parallel single-pixel imaging: A general method for direct–global separation and 3d shape reconstruction under strong global illumination. International Journal of Computer Vision **129**(4), 1060–1086 (2021)
14. Jiang, H., Yan, Y., Li, X., Zhao, H., Li, Y., Xu, Y.: Separation of interreflections based on parallel single-pixel imaging. Optics Express **29**(16), 26150–26164 (2021)
15. Jiang, H., Yang, Q., Li, X., Zhao, H., Xu, Y.: 3d shape measurement in the presence of strong interreflections by using single-pixel imaging in a camera–projector system. Optics Express **29**(3) (2021)
16. Jiang, H., Zhai, H., Xu, Y., Li, X., Zhao, H.: 3d shape measurement of translucent objects based on fourier single-pixel imaging in projector-camera system. Optics express **27**(23), 33564–33574 (2019)
17. Jiang, H., Zhou, Y., Zhao, H.: Using adaptive regional projection to measure parts with strong reflection. In: AOPC 2017: 3D Measurement Technology for Intelligent Manufacturing. vol. 10458, p. 104581A. International Society for Optics and Photonics (2017)

18. Kaiser, J.F.: Nonrecursive digital filter design using the i_0-sinh window function. In: Proc. 1974 IEEE International Symposium on Circuits & Systems, San Francisco DA, April. pp. 20–23 (1974)
19. Li, Y., Jiang, H., Zhao, H., Li, X., Wang, Y., Xu, Y.: Compressive parallel single-pixel imaging for efficient 3d shape measurement in the presence of strong interreflections by using a sampling fourier strategy. Optics Express **29**(16), 25032–25047 (2021)
20. Masselus, V., Peers, P., Dutre, P., Willems, Y.D.: Relighting with 4d incident light fields. Acm Transactions on Graphics **22**(3), p.613–620 (2003)
21. Nayar, S.K., Krishnan, G., Grossberg, M.D., Raskar, R.: Fast separation of direct and global components of a scene using high frequency illumination. In: ACM SIGGRAPH 2006 Papers, pp. 935–944 (2006)
22. O'Toole, M., Mather, J., Kutulakos, K.N.: 3d shape and indirect appearance by structured light transport. In: Proceedings of the IEEE Conference on Computer Vision and Pattern Recognition. pp. 3246–3253 (2014)
23. O'Toole, M., Raskar, R., Kutulakos, K.N.: Primal-dual coding to probe light transport. ACM Trans. Graph. **31**(4), 39–1 (2012)
24. Park, J., Kak, A.: 3d modeling of optically challenging objects. IEEE Transactions on Visualization and Computer Graphics **14**(2), 246–262 (2008)
25. Peers, P., Mahajan, D.K., Lamond, B., Ghosh, A., Matusik, W., Ramamoorthi, R., Debevec, P.: Compressive light transport sensing. ACM Transactions on Graphics (TOG) **28**(1), 1–18 (2009)
26. Sen, P., Chen, B., Garg, G., Marschner, S., Horowitz, M., Levoy, M., Lensch, H.: Dual photography. Acm Transactions on Graphics **24**(3), 745–755 (2005)
27. Sen, P., Darabi, S.: Compressive dual photography. In: Computer Graphics Forum. vol. 28, pp. 609–618. Wiley Online Library (2009)
28. Wang, Y., Zhao, H., Jiang, H., Li, X., Li, Y., Xu, Y.: Paraxial 3d shape measurement using parallel single-pixel imaging. Optics Express **29**(19), 30543–30557 (2021)
29. Xu, Y., Aliaga, D.G.: Robust pixel classification for 3d modeling with structured light. In: Proceedings of Graphics Interface 2007. pp. 233–240 (2007)
30. Xu, Y., Aliaga, D.G.: An adaptive correspondence algorithm for modeling scenes with strong interreflections. IEEE Transactions on Visualization and Computer Graphics **15**(3), 465–480 (2009)
31. Zhang, Y., Lau, D., Wipf, D.: Sparse multi-path corrections in fringe projection profilometry. In: Proceedings of the IEEE/CVF Conference on Computer Vision and Pattern Recognition. pp. 13344–13353 (2021)
32. Zhang, Y., Lau, D.L., Yu, Y.: Causes and corrections for bimodal multi-path scanning with structured light. In: Proceedings of the IEEE/CVF Conference on Computer Vision and Pattern Recognition. pp. 4431–4439 (2019)
33. Zhao, H., Xu, Y., Jiang, H., Li, X.: 3d shape measurement in the presence of strong interreflections by epipolar imaging and regional fringe projection. Optics express **26**(6), 7117–7131 (2018)
34. Zuo, C., Feng, S., Huang, L., Tao, T., Yin, W., Chen, Q.: Phase shifting algorithms for fringe projection profilometry: A review. Optics and Lasers in Engineering **109**, 23–59 (2018)
35. Zuo, C., Huang, L., Zhang, M., Chen, Q., Asundi, A.: Temporal phase unwrapping algorithms for fringe projection profilometry: A comparative review. Optics and lasers in engineering **85**, 84–103 (2016)